Journal of Alloys and Compounds 860 (2020) 158492

Contents lists available at ScienceDirect

Journal of Alloys and Compounds

journal homepage: www.elsevier.com/locate/jalcom

Polyol-mediated synthesis of Bi-deficient Mg^{2+}-doped sodium bismuth titanate and study of oxide ion migration behavior with functional properties

Pragati Singh[a], Raghvendra Pandey[b,*], Prabhakar Singh[a,*]

[a] Department of Physics, Indian Institute of Technology (BHU) Varanasi, Varanasi 221005, India
[b] Department of Physics, A.R.S.D. College, University of Delhi, New Delhi 110021, India

ARTICLE INFO

Article history:
Received 5 September 2020
Received in revised form 17 December 2020
Accepted 21 December 2020
Available online 24 December 2020

Keywords:
Oxygen ion conductor
Polyol mediated-synthesis
Sodium bismuth titanate
Electrolyte
Mg^{2+}-doping
Electrical conductivity
Solid oxide fuel cells

ABSTRACT

Sodium Bismuth Titanate, $Na_{0.5}Bi_{0.5}TiO_3$ (NBT) is considered as a probable lead-free piezoelectric material. But its acceptor-doped perovskite turns out as an outstanding oxide-ion conducting system with possible utilization in intermediate-temperature solid oxide fuel cells (IT-SOFCs). Also, the Bi-deficit Sodium Bismuth Titanate ($Na_{0.5}Bi_{0.5-x}TiO_{3-\delta}$) exhibits a notable oxide-ion conductivity. In the present investigation, the Bi-deficient and Mg^{2+}-doped Sodium Bismuth Titanate ($Na_{0.5}Bi_{0.49}Ti_{1-x}Mg_xO_{3-\delta}$; x = 0.00, 0.01, 0.02, 0.03) were first time synthesized via polyol mediated synthesis route at lower temperature with better surface area and good conductivity. The Mg^{2+} doping at Ti^{4+} site improved the sinterability and augmented the grain size. The structural, microstructural, textural and most importantly electrical properties were analyzed using XRD, Raman, FTIR, SEM, BET, TGA, and EIS techniques to gain understanding about effects of substitution of Mg^{2+} on structural behavior and electrical conductivity. We also explored the influence of Bi-deficient Mg^{2+}-substituted NBT compositions on the oxygen vacancies and ion migration behaviors. A correlation among the phase formation, conduction behavior and ion diffusion mechanism has been established for the Mg^{2+} substituted Bi-deficit NBT derived compositions. The conductivity was found to be maximum for NBT4902 composition over the entire temperature range. Though at the higher doping concentration of Mg^{2+} (x > 0.02), conductivity was found to slightly decrease.

1. Introduction

Over the past few decades, climate variability, environmental degradation, power outages due to energy shortage issues have compelled researchers to develop efficient energy conversion and storage devices. Many of these devices are utilizing ion-conducting materials to diffuse the mobile ions. Out of these ion-conducting materials, oxide ion conductors have been extensively explored because of their technological implication in the number of electrochemical devices such as solid oxide fuel cells (SOFCs), pumps, oxygen sensors, oxygen and separation membranes catalysts etc. [1–6]. Up to now, substantial attempts are made to discover oxygen ion conductors, like stabilized ZrO_2, doped CeO_2, δ-Bi_2O_3, Sr^{2+} and Mg^{2+} incorporated $LaGaO_3$, $CeNbO_{4.25}$, Silicate apatite's, $NdBaInO_4$ and Ba_3NbMoO_8 [6–17]. Moreover, in these materials, the oxygen ion conduction can be understood by means of interstitial oxygen ions migration and/or migration of oxygen vacancies inside the crystal that may result in higher activation energy due to the infringement and reconstitution of associated chemical bonds. Hence, these oxide-ion conductors generally require high operating temperature in order to get improved ionic mobility. Yttria stabilized zirconia (YSZ) is a widely stable oxide ion conducting ceramic electrolyte but demonstrates high conductivity only at elevated temperatures (above 800 °C). Sm/Gd doped ceria (SDC/GDC) and Sr^{2+} and Mg^{2+} incorporated $LaGaO_3$ oxides (LSGM) with higher conductivities in the moderate-temperature range were also recognized as possible electrolytes [13,14]; though, these ceramics comprises many kinds of rare earth metals and expensive materials. Also, the wide range of stability and mixed conduction is an immense problem for Sm/Gd doped ceria. Recently, Li et al. reported that $Na_{0.5}Bi_{0.5}TiO_3$ (NBT) as a rare-earth free perovskite-based oxide-ion conductor which was previously considered as lead-free piezoelectric material [18]. A slight deviation in the A site non stoichiometry can lead to three order of change in conductivity [19]. The oxide-ion conductivity in

* Corresponding authors.
E-mail addresses: raghvendra@arsd.du.ac.in (R. Pandey), psingh.app@iitbhu.ac.in (P. Singh).

https://doi.org/10.1016/j.jallcom.2020.158492
0925-8388/

the NBT based ceramics could be further enhanced via Bi-deficiency and a little amount of Mg^{2+}-doping at Ti site, e.g. $Na_{0.5}Bi_{0.49}Ti_{0.98}Mg_{0.02}O_{2.965}$, which was due to the highly polarized Bi^{3+} cations, feeble Bi-O bond and modified oxygen-vacancy concentrations. Its conductivity reaches ~0.01 S cm^{-1} at 600 °C, which is comparable to the well-known oxygen-ion conductors $La_{0.8}Sr_{0.2}Ga_{0.8}Mg_{0.2}O_{2.8}$ and $Ce_{0.8}Gd_{0.2}O_{1.9}$ at this temperature [20–22].

Several researchers have attempted to explain the cause of high oxide-ion conductivity, local atomistic configurations, defects formations mechanism, anions migration mechanism of NBT and its derivative compositions by the first principle and DFT based calculations [23–29]. In these studies, the origin of high ionic conductivity was supposed to originate from oxygen vacancies generation due to Bi-deficit content in addition to high oxide ion mobility. This high mobility may be arising due to highly polarizable Bi^{3+} ion that is because of weak Bi–O bonds and $6s^2$ lone pair electrons. This also provides ion diffusion pathways with fewer transport barriers [30]. Moreover, the experimental evidence to demonstrate the adequacy of the highly polarized Bi^{3+} cations to generate high oxide-ion mobility is not very profound. Furthermore, Lu et al. have studied the oxygen vacancy formation mechanism along with transport properties in NBT crystal at higher temperatures [31]. Although, NBT and accepter doped Bi deficient NBT compositions are mostly synthesized by solid-state reaction routes and a very few reports of synthesis of NBT based compositions are found via solution-based techniques. Reshetnikova et al. have synthesized the NBT based ferroelectric compositions employing the hydrothermal method with sodium hydroxide solution and studied its phase formation behavior [32]. Synthesis of Sodium and Potassium Bismuth Titanates (NBT/KBT) via hydrothermal method is also reported by the Lencka et al. and they considered the yield diagrams and stability of the studied systems and also optimized the processing parameters for investigated KBT and NBT systems [33]. Kim et al. have synthesized the Bismuth Sodium Titanate nano-powders by sol-gel method and studied the structural parameters of the compositions [34]. A few more reports of solution-based synthesis of NBT derived compositions were also found, but these reports generally explored the structural and processing parameters of the investigated systems [35–42] Nevertheless, to the best of our knowledge, there is no report of the synthesis of NBT and its derivative compositions via polyol mediated route with the exploration of detailed structural investigation in correlation to electrical properties and ion migration analysis. In the present work, we have synthesized NBT derivative compositions, $Na_{0.5}Bi_{0.49}TiO_{3-\delta}$, $Na_{0.5}Bi_{0.49}Ti_{0.99}Mg_{0.01}O_{3-\delta}$, $Na_{0.5}Bi_{0.49}Ti_{0.98}Mg_{0.02}O_{3-\delta}$ and $Na_{0.5}Bi_{0.49}Ti_{0.97}Mg_{0.03}O_{3-\delta}$ employing polyol mediated synthesis method at relatively lower processing temperature in comparison to solid-state reaction route. In polyol mediated synthesis, ethylene glycol molecules (EG) acts as a capping agent in addition to reaction media. Therefore, we can get fine particles with homogeneous phase, narrow particle distribution and better surface area at relatively lower temperatures. The effects of partial substitution of Mg^{2+} on the Ti^{4+} site with oxygen migration in correlation with structural distortions and electrical conductivity has been systematically discussed for all the investigated compositions.

2. Experimental

2.1. Synthesis

Here onwards, $Na_{0.5}Bi_{0.49}TiO_3$, $Na_{0.5}Bi_{0.49}Ti_{0.99}Mg_{0.01}O_3$, $Na_{0.5}Bi_{0.49}Ti_{0.98}Mg_{0.02}O_3$, $Na_{0.5}Bi_{0.49}Ti_{0.97}Mg_{0.03}O_3$ oxides are abbreviated as NBT4900, NBT4901, NBT4902 and NBT4903, respectively. High purity grade reactants of Na_2CO_3 (99.8%, Alfa Aesar), Bi_2O_3 (99.9%, SRL), Titanium Isopropoxide ($C_{12}H_{28}O_4Ti$) (99.95%, Alfa Aesar), MgO (99.9%, Alfa Aesar) were weighed as per required molar concentration. Then the weighed compounds as Na_2CO_3 was dissolved into water, Bi_2O_3 and MgO were dissolved separately into HNO_3. The specific molar concentration of Titanium Isopropoxide was also taken separately into the measuring cylinder. Then these solutions were mixed in a conical flask and kept for magnetic stirring at 80–90 °C. After some time, double stage distilled water was added three to four times to eradicate the surplus acids. In this solution, 100 ml of EG was added into the five gram of urea (NH_2CONH_2) dissolved double-distilled water. In order to achieve the uniform mixing of the solution, the solution was kept for constant stirring about 2 h. After that, this mixed solution was heated around ~100–120 °C to get the white precipitates. In this nano-powder synthesis approach, EG molecules behave as a solvent in addition to capping agent for reaction media. As the nucleation begins, neighboring EG molecules cap smaller particles which moderate the particle growth rate. This also helps in hindering the agglomeration process of particles. The EG dielectric media of reaction also supports in controlling particle size. The obtained precipitate was eroded 2–3 times in ethanol in order to eliminate the extra EG and then kept for two days at room temperature to dry it. And after crushing, the as-prepared compositions were annealed at 500 °C in the air for 4 h. In the burning process, EG (the capping agent) is eliminated as carbon dioxide and water vapor phases. Thus, the uncapped particles were obtained and hence the growth of particles occurs. The obtained powders were mixed with one drop of 2 wt% PVA solution and ground into fine powders to make the disks shapes pellets under the hydraulic pressure of 150 MPa. Thus, these pellets were sintered in the ambient atmosphere at 800 °C for 4 h in a muffle furnace. Fig. 1.

2.2. Characterizations

The phases of the annealed powder were analyzed by X-ray diffraction (XRD, Rigaku Miniflex II desktop) with Cu-$K_{\alpha 1}$ radiation in the 2θ range of 20°–80°. All the compositions were then sintered at 800 °C in the air with a stay time of 4 h. The phases of sintered pellet were determined by XRD to observe the second phase, if any, after firing at higher than calcination temperature. The specific surface area of calcined powders was determined by BET method through Quantachrome Instruments (ASI-CI-11) of accelerated surface area and porosimetry system using N_2 adsorption-desorption isotherms. The microstructure of the sintered specimens (polished with emery papers) was observed by scanning electron microscope (EVO-Scanning electron microscope MA15/18 instrument). The average grain size of each sample was measured by Image *J* software. DSC/TGA was performed using the Perkin Elmer instrument in N_2 atmosphere up to 750 °C. The room temperature Raman spectra of all four compositions were recorded using Renishaw reflex micro Raman spectrometer. FTIR study was performed in the range of 400–4000 cm^{-1} using Perkin Elmer FTIR spectrometer (RXI) in KBr media. Both sides of the pellets were polished and thermally etched to apply the high-temperature Ag paints. The AC impedance data of all four sintered compositions were collected from 200 to 600 °C by a DC 2-probe Wayne-Kerr LCR meter (6500 P) as a function of frequency in ambient atmosphere.

2.3. Bond valance energy calculations (BVELs)

The bond valance based energy calculations for test oxide ion (O^{2-}) was calculated in order to investigate the oxide ion diffusion pathway and energy migration barrier. The Rietveld refined parameters obtained from full proof software were used for BVE calculations. The energy calculation was carried out using softBV [43,44] program with the spatial resolution of 0.1 Å. The crystal structure and energy landscape were visualized using VESTA software [45].

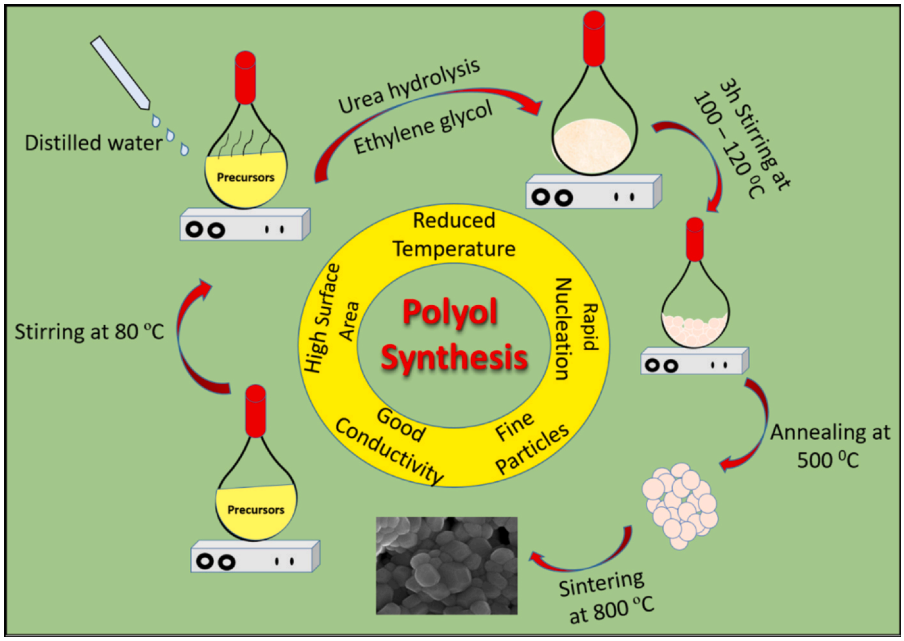

Fig. 1. Schematics of polyol mediated synthesis of NBT derivatives.

3. Results and discussion

3.1. Structural analysis

Fig. 2 shows the room temperature X-ray diffractograms of $Na_{0.5}Bi_{0.49}Ti_{(1-x)}Mg_{(x)}O_{3-\delta}$ (x = 0.00, 0.01, 0.02, 0.03) samples. No traces of any secondary phase are observed in the resolution limit of the XRD. All the samples are indexed according to the rhombohedral symmetry and *R*3*c* space group [18]. A weak superlattice reflection present in all the studied compositions at 2θ~38.5° represents the antiphase rotation of TiO_6 octahedra. To observe it very critically, we have also done Rietveld refinement of all the sample using FullProf Suite package with Pseudo–Voigt peak profile. Fig. 3 depicts the refinement plots, and the goodness of fit (χ^2) lies in the appreciable range. Fig. 2(b) shows the crystal structure of NBT generated using refined cell parameters and vesta software [45]. The variation of lattice parameters is shown in Fig. 4(a) and the other refinement parameters are listed in the supplementary section (Table. S1).

It is noticeable that the lattice parameter *c* increases with Mg^{2+} doping up to 2% of Mg^{2+} doping, i.e. NBT4902 and then after it decreases whereas lattice parameter *a* increases up to 1% of Mg^{2+} doping and then decreases. Unit cell volume is also increasing with Mg^{2+} doping up to 2%, as Mg^{+2} (r = 0.72 Å) cation have larger radii than that of Ti^{+4} (r = 0.602 Å) [46]. Sodium bismuth titanate (NBT) sample possesses local octahedral tilting about the threefold

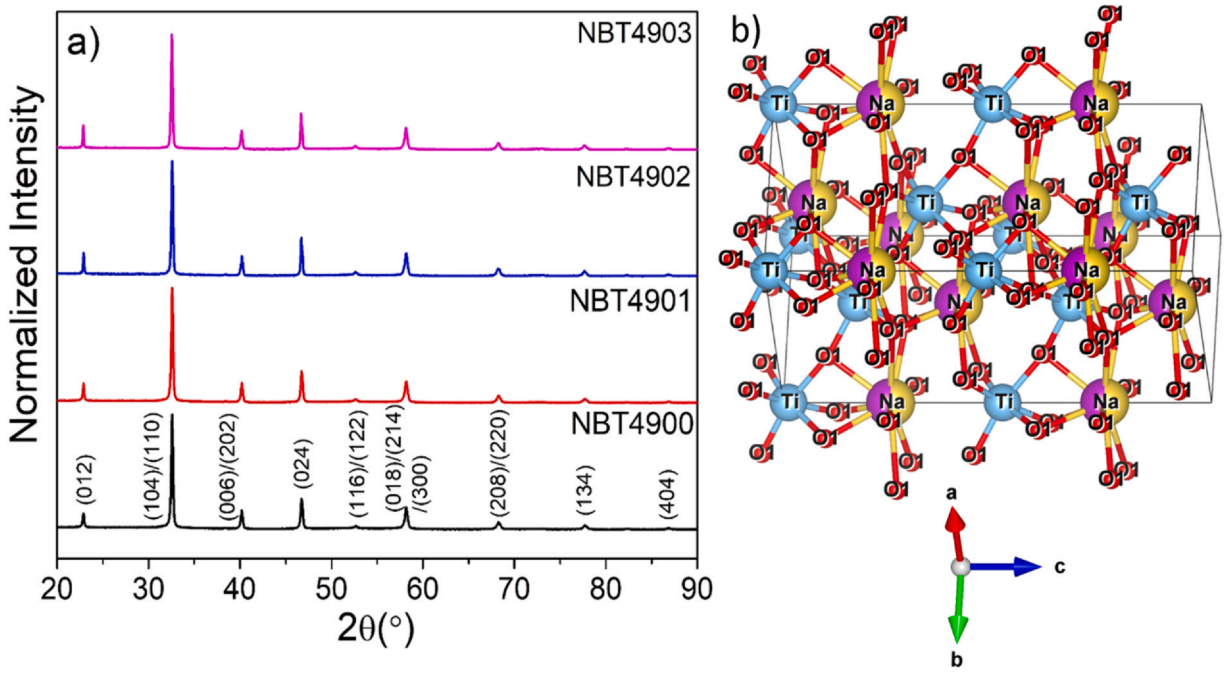

Fig. 2. (a) X-ray diffractogram pattern of $Na_{0.5}Bi_{0.49}Ti_{(1-x)}Mg_{(x)}O_{3-\delta}$ (x = 0.00, 0.01, 0.02, 0.03) (b) Representative crystal structure in 3D view.

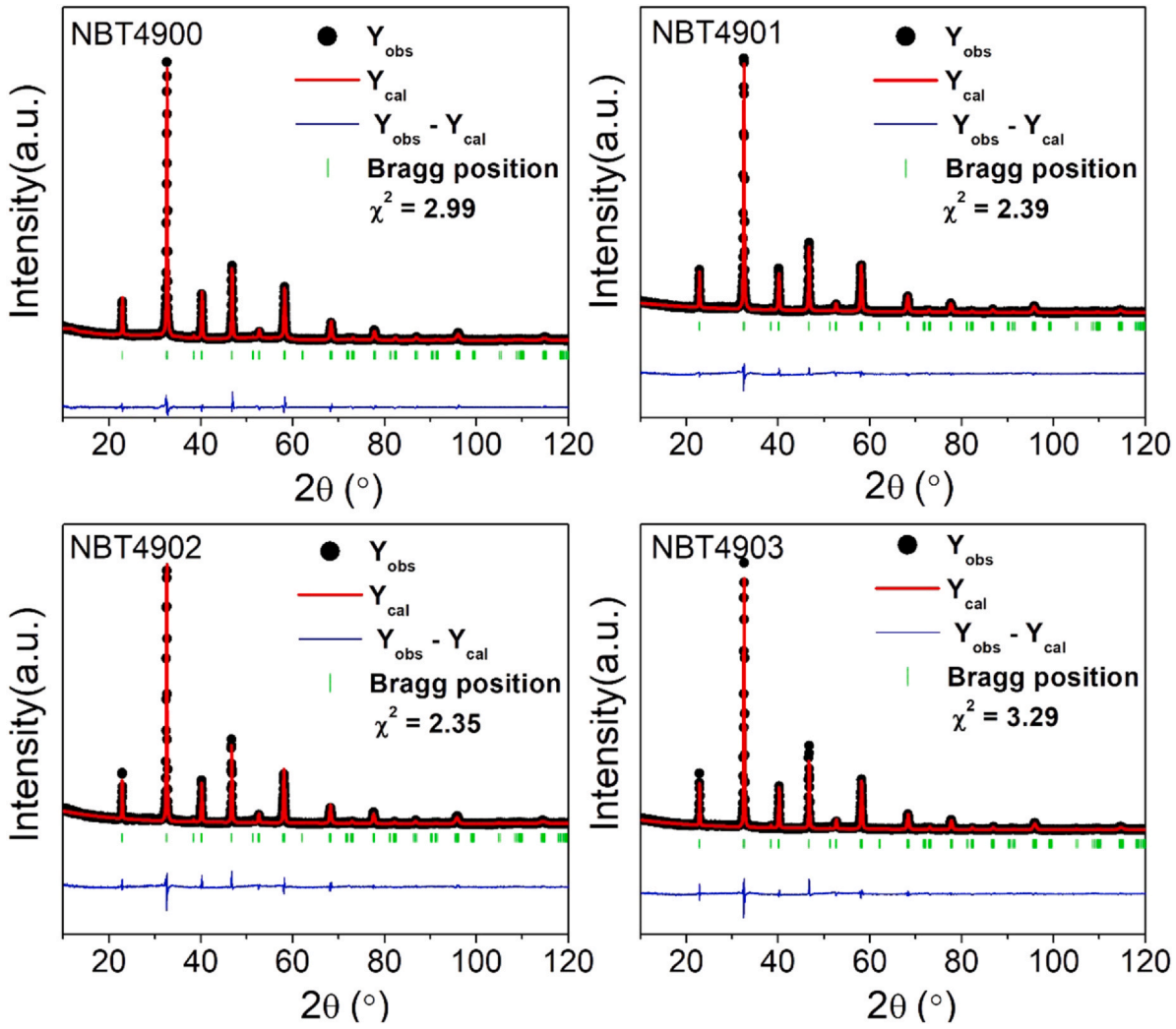

Fig. 3. Rietveld refinement pattern of NBT4900, NBT4901, NBT4902 and NBT4903. Black circles represent the experimental data, and red lines are the fit. Green vertical bars personify the Bragg's reflections and blue line at the bottom represents the difference between the observed and fitted data. (For interpretation of the references to colour in this figure legend, the reader is referred to the web version of this article.)

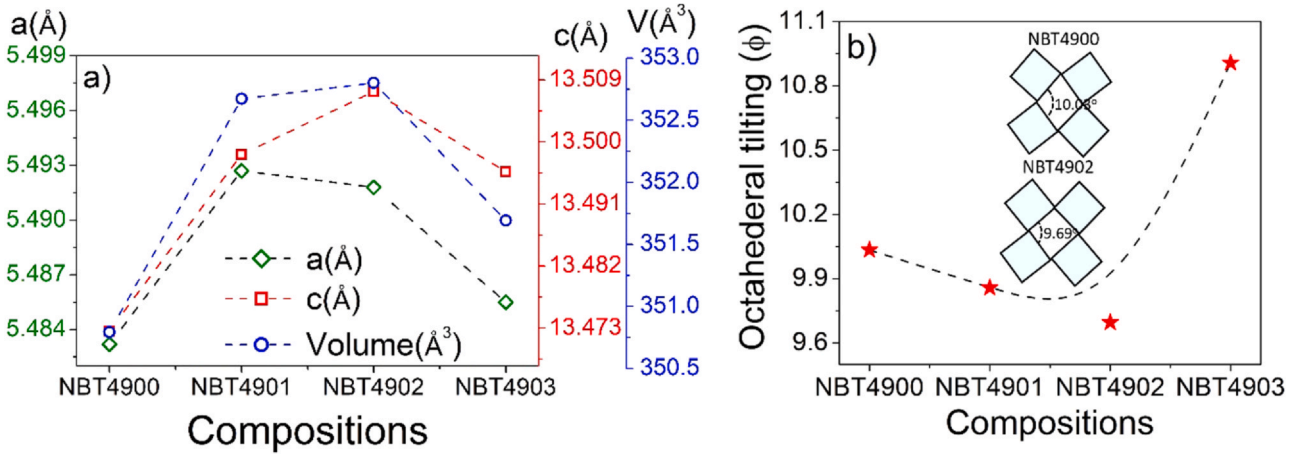

Fig. 4. (a) Variation of lattice parameters *a*, *c* and, volume (b) Octahedral tilting (ϕ) with composition obtained from Rietveld refinement.

pseudo-cubic axes ($a^-a^-a^-$) and affects the oxide ion motion in the system [47]. Fig. 4(b) depicts the variation of octahedral tilting (ϕ) in the sample. This octahedral tilting (ϕ) is due to the bending of TiO_6 octahedra. It is given by the relation:

$$cos^2 \Phi = \frac{2 - 2cos\theta}{cos\theta + 5} \quad (1)$$

where ϕ is the octahedral tilting and θ is the bond angle between Ti–O–Ti. The tilting is minimum for NBT4902 sample. The average

Table 1
Average crystallite size, micro-strain and density of the investigated compositions.

Composition	Average crystallite size (nm)	Micro-strain	Density (g/cm^3)
NBT4900	41	1.27×10^{-4}	5.2
NBT4901	39	1.72×10^{-4}	5.4
NBT4902	36	1.95×10^{-3}	5.6
NBT4903	34	2.13×10^{-3}	5.6

value of crystallite size and micro-strain was deduced using the Williamson Hall method:

$$\beta cos\Theta = \frac{k\lambda}{D} + 4\varepsilon sin\Theta \quad (2)$$

where β is the line broadening (FWHM), k is the shape factor ($k = 0.9$), λ is the wavelength of X-ray, D is average crystallite size, ε is strain and Θ is the Bragg's diffraction angle [48]. Estimated values are listed in Table 1. It is clear from the table that both the Crystallite size and microstrain are showing the opposite trend, suggesting decrease in the crystallite size and increase in the microstrain with the increase in Mg^{2+} concentration.

3.2. Migration pathway analysis

The bond valance energy landscape for a test oxide ion was calculated using softBV software [49]. The energy of oxide ion was calculated for each grid point with the resolution of 0.1 Å. Fig. 5(a) represents the Bond valence energy landscape (BVEL) of all the investigated system at the iso-surface value of 2.5 eV. On the basis of BVE based calculations, the migration pathways were made for the fully relaxed initial and ending structures (extraneous) from linearly interpolated images. Hence, oxygen migration energy barrier can be calculated as using the relation, $E_a = E_{max} - E_{min}$, where E_{max} and E_{min} are the highest and the lowest energy iso-surface values along the diffusion pathway of initial and ending structures (extraneous), respectively. The Room Temperature rhombohedral structure was considered in the BVEL calculations [23].

Form Fig. 5(a), it is revealed that at the same iso-surface value, the iso-surface migration channels are more in Mg^{2+}-doped compositions as compared to undoped one (NBT4900). The BVE landscape for connected and extraneous iso-surface in the b-c plane are shown in Fig. 5(b). The iso-surface forms a continuous channel along any particular crystallographic direction and reflects the migration energy along that path, and the narrowest path corresponds to the maximum barrier along that channel [50]. Different iso-surface along different orientation suggests anisotropic diffusion in the structure. The energy migration barrier for oxide migration in NBT4900 is ~0.68 eV and is found to slightly increase with Mg^{2+} doping, but the number of intermediate pathways segment also increases for Mg^{2+}-doped compositions. Both the stable iso-surface energy and migration energy barrier increases for Mg^{2+}-doped compositions. In perovskites, the anion conduction pathway is assumed to arise by a hopping mechanism wherever migrating anions passes through the bottleneck or opening of the critical radius of a triangle through saddle points which are in between A-site and B-site ions [18]. Here, the migration of oxide ion occurs via edges of TiO_6 octahedra via -O1-O1- pathways and through interstitials and saddle points inside the unit cell of the crystal. Further reaction coordinate pathway analysis (Supplementary Fig. S1) also depicts that NBT4900 have less number of intermediate pathway segments for migration as compared to Mg^{2+}-doped compositions. The possible cause for the increase in the migration barrier with Mg^{2+} doping is electrostatic and elastic interaction between dopant and oxygen vacancies. Thus, the oxide-ion migration barriers in NBT and derivative compositions are vastly dependent on the local symmetry's phases, the A- and B-site cation order, tilt configurations and the various oxide-ion diffusion pathways.

3.3. Surface morphology study

The SEM micrographs of the fractured cross-section are shown in Fig. 6. All the samples appeared to be dense, and the results are in accordance with the bulk density measured from Archimedes density kit (listed in Table 1). Although the XRD pattern suggests pure phase sample, SEM micrographs of NBT4903 shows dense phase with some few dispersed particles. The grains consist of non-uniform morphology, and the average grain size was measured using Image *J* software. The grain size is found to increase with Mg^{2+} doping. This increase in the grain size could be attributed to the grain boundary roughening. It is a well-reported fact that oxygen vacancy induces surface and grain boundary roughening as a result of increased entropy [27]. So, the formation of oxygen vacancy may be the reason for grain boundary roughening. Thus, the grain morphology variation also supports the structure-property correlation.

3.4. Thermogravimetric analysis

The TGA curve of the studied samples in the temperature range of 30–750 °C is shown in Fig. 7. An initial increase in mass flow, followed by continuous mass loss, is observed. Multiple kinks at temperature ~100, 250 and 460 °C are also observed showing multistage decomposition reaction. Kink at ~100, 250 and 460 °C corresponds to H_2O, O_2 and CO_2 loss, respectively. The peak in the temperature range of 30–150 °C is due to the moisture adsorbed on the surface of particles [42]. As the samples were sintered at high temperature ~ 800 °C, so all the hydrocarbon will get driven off. Further, the X-ray diffractograms of all the samples are also showing clear phase. So we can conclude that the hump at ~100 °C is due to the moisture adsorbed on the powder sample. To further confirm this, we have added room temperature FTIR measurement in the supplementary section (Fig. S3).

The kink observed ~520 °C is used to calculate oxygen content in the sample [51]. The oxygen vacancy calculated using the following reaction (Kroger-Vink notation)

$$2Bi_{Bi}^{X} + 3O_{O}^{X} \rightarrow 2V_{Bi}^{''} + 3V_{\ddot{O}} + Bi_2O_3 \quad (3)$$

$$MgO \xrightarrow{TiO_2} Mg_{Ti}^{''} + V_{\ddot{O}} + O_O^X \quad (4)$$

are listed in Table 2. The negative sign represents the oxygen-deficient sample, and the weight loss is mainly because of the loss of lattice oxygen [46]. Mg^{2+}-doped sample is more oxygen-deficient because of the charge compensation.

3.5. Raman spectroscopy study

Raman spectroscopy is a sensitive technique to understand crystal symmetry, structural distortion and its relation with doping. Normalized Raman spectrum of the studied samples is shown in Fig. 8. The number of Raman modes obtained after deconvoluting the data is as per the Raman modes prescribed by Bilbao Crystallography [52] for R3c symmetry (Fig. 9). All the modes are broad, showing the polycrystalline nature of the sample. Spectra of all the samples were fitted to Gaussian-like shape using origin software with 13 peaks, and the fitted parameters such as FWHM, Peak intensity, area under the curve were calculated. Major regions observed in the spectrum are categorized as:

1. **Band A** (80–200) cm^{-1}: It is associated with the Bi–O and Na–O bond and contains three regimes assigned to E(LO1), A_1(TO1) and A_1(L02) mode [53]. Mode observed at the lower frequency

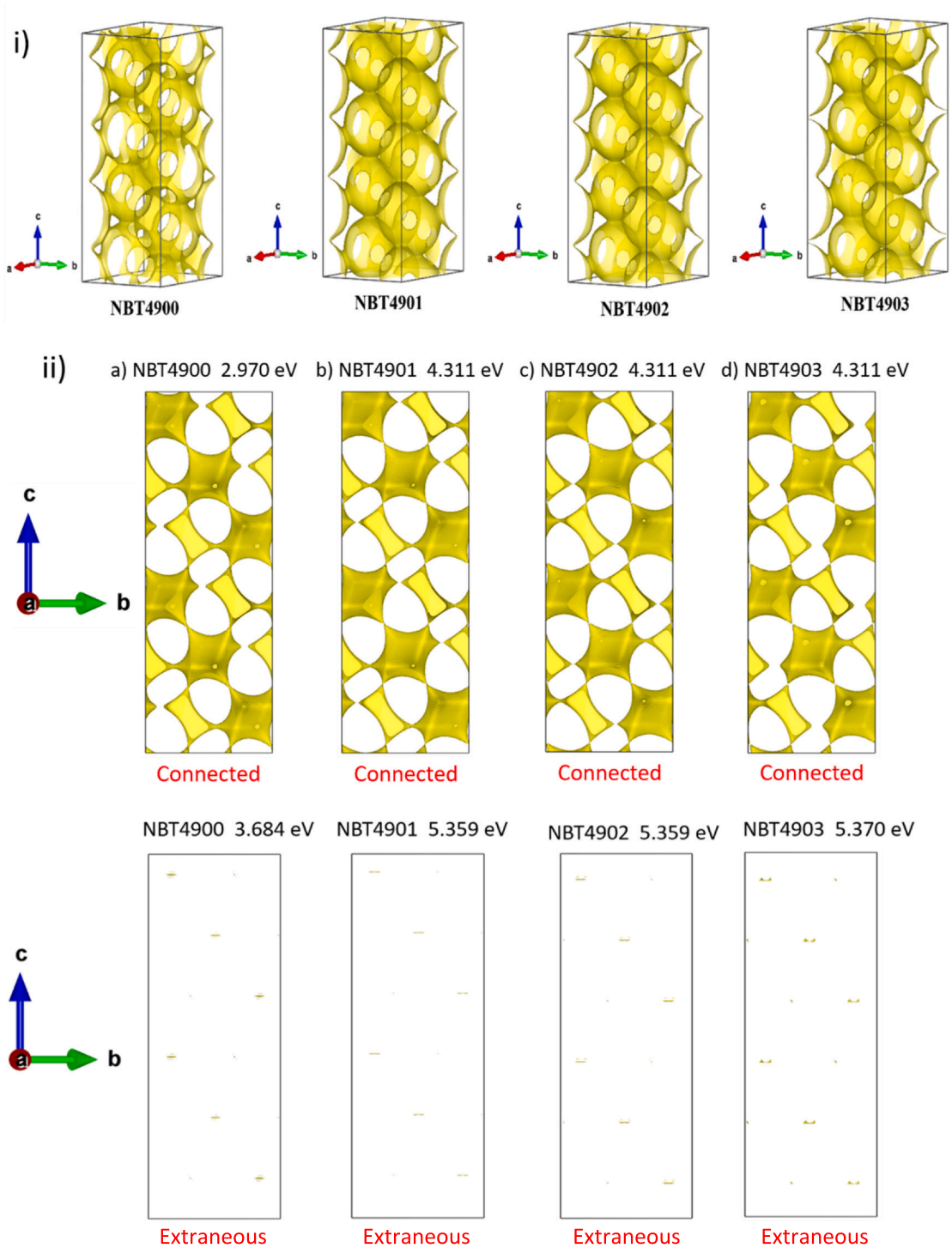

Fig. 5. (a) Bond valence energy landscape (BVEL) of all the investigated system at the iso-surface value 2.5 eV. (b) Oxide ion migration channel of studied composition in the b-c plane obtained from BVE method. Presence of yellow surfaces means the presence of the migration pathway channels, and the extraneous iso-surface represents the absence of migration pathways channels. (For interpretation of the references to colour in this figure legend, the reader is referred to the web version of this article.)

(109–134 cm^{-1}) is usually associated with Bi–O bond because of its higher atomic mass and the mode observed at higher frequency (155–187 cm^{-1}) is related to Na–O bond [54].

2. **Band B** (200–400) cm^{-1}: It is associated with the Ti–O vibrations, and it also contains four regimes assigned to A_1(TO3), E(TO4), E (TO5) and A_1(LO5) mode.
3. **Band C** (400–660) cm^{-1}: It is associated with the vibration of oxygen. Modes observed in this regime are assigned to A_1(LO7), E (TO8), and E(LO8).
4. **Band D** (660–930) cm^{-1}: These bands are associated with the presence of the oxygen vacancies and are the most important feature of room temperature Raman spectra. Presence of such a band was first observed by Selvamani et al. [55]. Modes found in this regime are assigned to E(LO9), A_1(TO9), and A_1(LO9).

To investigate the doping effect on the structure, FWHM and Peak intensity of all the modes were analyzed. Fig. 10 depicts the variation of the FWHM of E(TO4) and E(LO9) mode. With the increases in Mg^{2+}

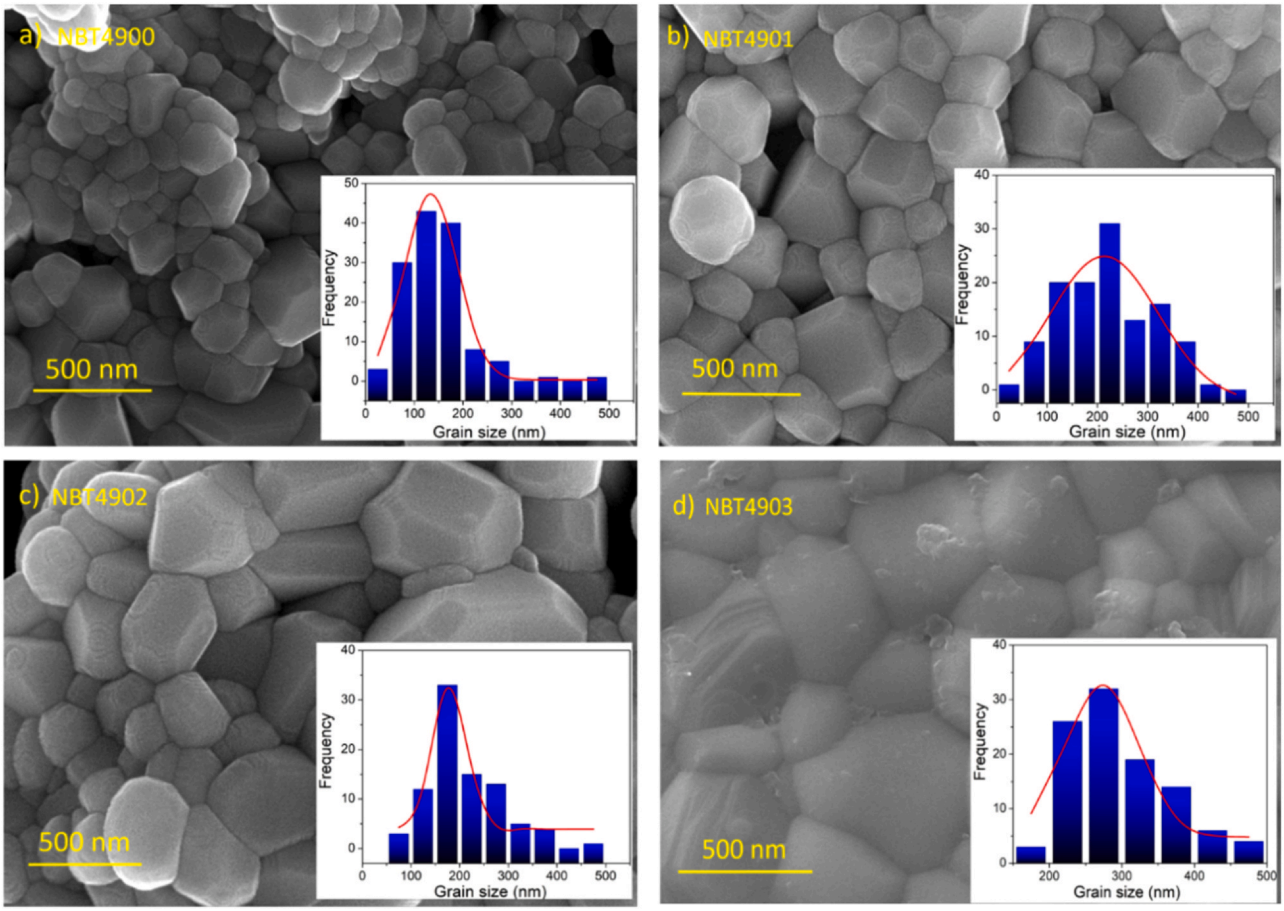

Fig. 6. (a–d) SEM micrographs of the sintered samples. Inset shows grain size distribution histogram.

concentration, FWHM of E(LO9) mode increases, suggesting an increase in the oxygen vacancies. Simultaneously there is an increase in FWHM of E(TO4) mode up to 2% Mg^{2+} followed by a decrease for higher doping concentration, suggesting structural distortion in the Ti–O bond of TiO_6 octahedra is maximum for NBT4902.

Hence, the interplay between the oxygen vacancies and TiO_6 octahedron distortion has appeared, which may affect the conductivity of the specimens with the Mg^{2+} doping.

3.6. Brunauer-Emmett-Teller (BET) analysis

Nitrogen adsorption-desorption isotherm as the function of relative pressure is shown in Fig. 11. According to IUPAC classification, all the isotherm depicts type IV hysteresis loop and are associated with the mesoporous materials [56]. Brunauer, Emmett and Teller (BET) gave the method to determine specific area and porosity given by

$$\frac{1}{\upsilon[(p_0/p)-1]} = \frac{c-1}{\upsilon_m}\left(\frac{p}{p_0}\right) + \frac{1}{\upsilon_m c} \quad (5)$$

$$c = exp\left(\frac{E_1 - E_L}{RT}\right) \quad (6)$$

$$V_{liq} = \frac{P_a + V_{ads} + V_m}{RT} \quad (7)$$

where υ is the volume of adsorbed gas, υ_m is the volume of adsorbed as monolayer, p_0/p is the relative pressure, c is BET constant, E_1 is the heat of adsorption of the first layer, and E_L is adsorption heat for the second and higher layers, V_{liq} is the volume of N_2 in the pore, V_{ads} is the volume of gas adsorbed, V_m is the molar volume of liquid adsorbed, P_a is ambient pressure and T is temperature [21]. The lower part of the adsorption curve (till relative pressure 0.2) is used for specific surface area calculation, and the entire adsorption-desorption range is used for pore analysis. Table 3 depicts the calculated specific surface area, pore size and volume of the studied composition. The specific surface area of all the samples lies between 100 and 160 m^2/g. This can also be seen from the Table 3, the surface area is maximum for NBT4902.

Above results suggest that the polyol method produces mesoporous NBT material with high specific surface area, indicating its thermal stability. This high surface and low porosity are the important parameters for its application as electrolyte material in solid oxide fuel cells to produce optimum power density.

3.7. Electrical conductivity study

The representative AC impedance Nyquist plots at 500 °C for all the studied compositions are shown in Fig. 12(a). Characteristically, a Nyquist Cole-Cole curve contains three arcs, that are usually associated with the grain, grain boundary, and electrode-related impedance responses in high, intermediate and lower frequency regime, respectively. In the present investigation, a depressed semicircle corresponding to bulk impedance is observed due to the limited frequency range of the equipment. From Fig. 12 (a) it can be seen that the resistance of the sample is decreasing with the increase in Mg^{2+} concentration up to 2% and then after decreases for 3% Mg^{2+} substitution. The Z-view electrical equivalent circuit is also shown in the inset of Fig. 12 (a). An equivalent circuit consisting of two parallel combinations of resistance and constant phase element (CPE) was found to best fit the experimental data. The fitting was

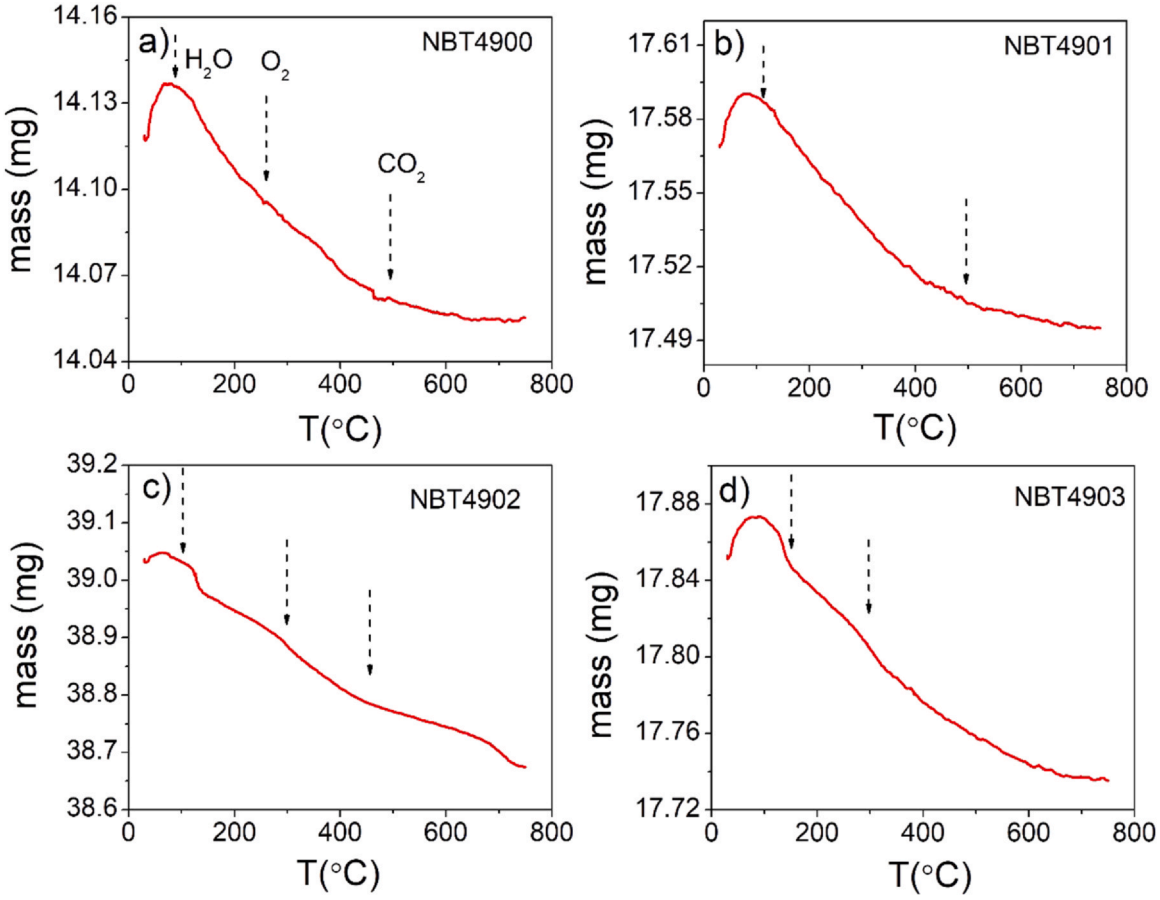

Fig. 7. (a–d) TGA of $Na_{0.5}Bi_{0.49}Ti_{(1-x)}Mg_{(x)}O_{3-\delta}$ (x = 0.00, 0.01, 0.02, 0.03) in N_2 atmosphere.

Table 2
Oxygen vacancy estimated from TGA data and electrical conductivity.

Sample	Oxygen deficiency δ	Conductivity (S/cm) at 600 °C
NBT4900	−0.0048	0.084×10^{-2}
NBT4901	−0.0074	0.159×10^{-2}
NBT4902	−0.0919	0.279×10^{-2}
NBT4903	−0.0209	0.129×10^{-2}

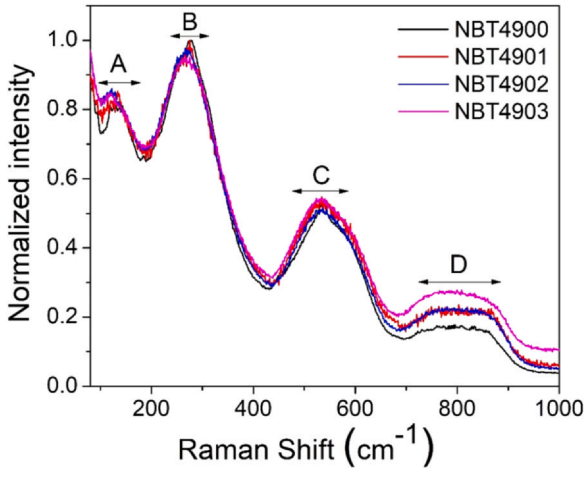

Fig. 8. Room temperature Raman spectra of the studied compositions.

done in the frequency range of 24 Hz to 1 MHz. Each plot contains two semicircles. The arc at higher frequency corresponds to the grain conduction, and the arc at the lower frequency corresponds to the grain-boundary conduction. The grain-boundary (R_{gb}) and the grain resistance (R_g) are calculated by the intercept of these arc on the X-axis and both contributes in total resistance of the samples. The total conductivity was calculated taking the bulk responses of the samples using the formula $\sigma_t = \frac{t}{A \times R_t}$ where, σ is the conductivity, R_t (=R_g + R_{gb}) is the total resistance, t is the thickness, and A is the area of the pellet. Arrhenius plots for the total conductivity results are shown in Fig. 12 (b) for all the compositions. Fig. 12 (b) is linearly fitted with the Arrhenius relation as per the following equation:

$$\sigma_t T = \sigma_0 \exp\left(\frac{-E_a}{k_B T}\right) \tag{8}$$

where σ_0 is the pre-exponential factor, T is temperature, k_B Boltzmann's constant and E_a is the activation energy. The electrical conductivity of NBT4900 is consistent with the earlier reported results of similar systems [28,57]. And on substituting 1–2% of Mg^{2+}, an increase in the conductivity is observed. However, on further adding Mg^{2+} to 3% decreases the conductivity because of the solid solubility limit of the Mg^{2+} on the Ti site, which is ~1–2% [58]. The conductivity may also get lower at higher Mg^{2+}-doping due to the Mg^{2+} defect pair associations leading to a reduced effective concentration of mobile vacancies [24]. The complex formation reaction for this defect pair association could be as follows:

$$Mg''_{Ti} + V_O^{\cdot\cdot} \longleftrightarrow (Mg''_{Ti} - V_O^{\cdot\cdot})^{\times} \tag{9}$$

The value of activation energy for the studied samples in the temperature range of 500–600 °C are shown in Fig. 12(c). Comparison of activation energy suggests that the Mg^{2+}-doped sample shows higher activation energy. Despite the increase in the activation energy, Mg^{2+}-doped bismuth deficient samples are showing

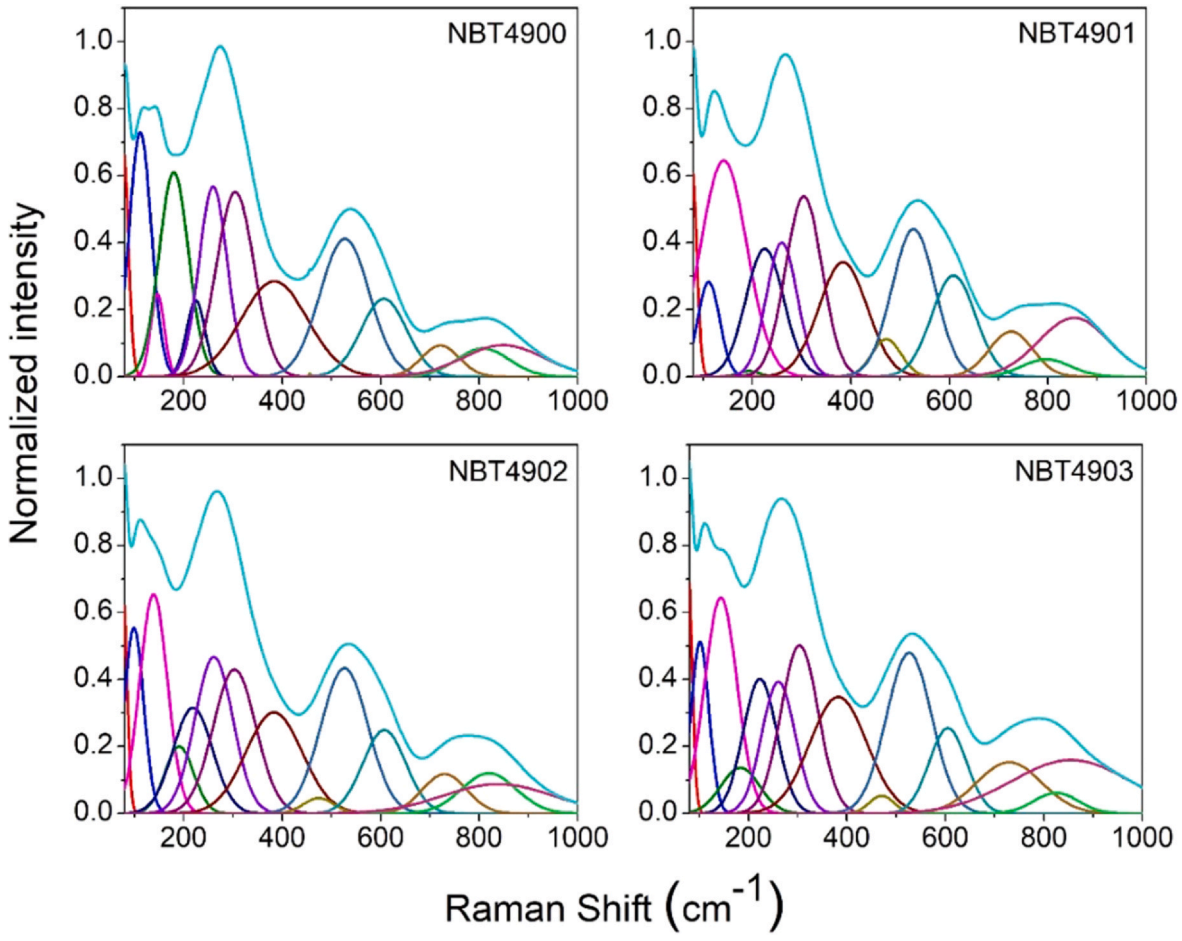

Fig. 9. Deconvoluted Raman spectra using 13 peaks showing the presence of R3c symmetry.

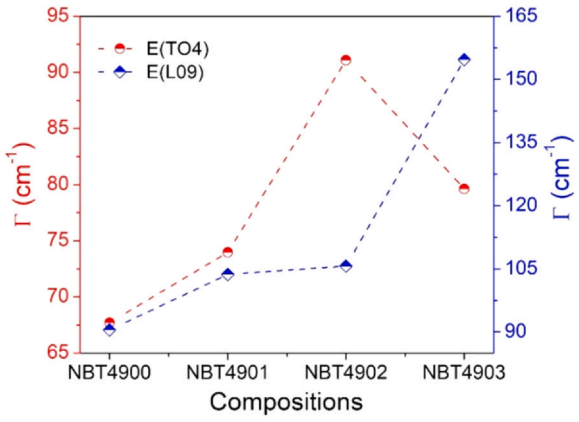

Fig. 10. FWHM variation in Raman spectra for E(TO4) and E(LO9) mode of all the investigated compositions.

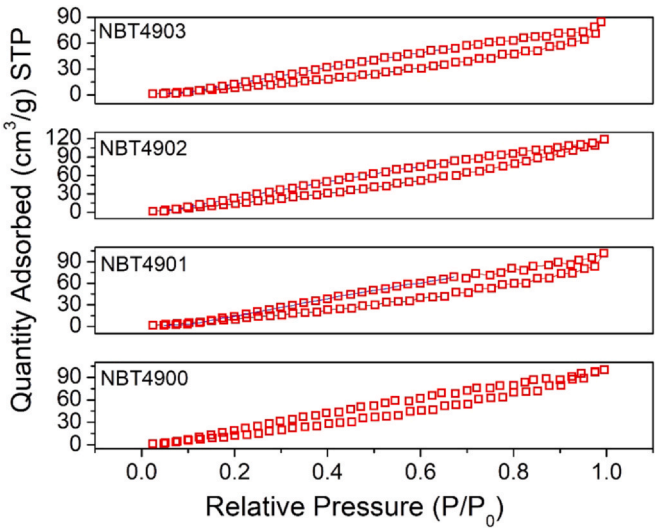

Fig. 11. BET nitrogen adsorption isotherm as a function of relative pressure.

higher oxide ion conductivity. The high activation energy for Mg^{2+}-doped compositions is correlated with the migration barrier analysis, as we have discussed in the structural section. A change in activation energy, E_a from ~0.7 to ~0.9 eV above 500 °C to below 500 °C is possibly due to structural transition from tetragonal (T) to cubic (C) phases around this temperature [59]. Although, the room temperature rhombohedral phase is coexisted with tetragonal (T) phases in the temperature range from ~250 to ~450 °C. For this phase regime, the activation energy may consist of the migration energy along with the association energy of the defect pairs $(Mg''_{Ti} - V_O^{\cdot\cdot})^{\times}$and $(V'''_{Bi} - V_O^{\cdot\cdot})'$associates [54]. A similar kind of trend was also observed in the previous literature [60]. This behavior confirms that the conductivity has to do more with the oxygen ion concentration along with migration energy barrier [24,61]. These results are also evident from the electron density analysis (discussed in the Supplementary section).

The Mg^{2+}-substitution at Ti-site in NBT is useful in letting down the resistance responses offered by means of grain boundaries. As

Table 3
BET surface area, pore size and pore volume of all investigated compositions.

Sample	BET surface area (m^2/g)	Pore size (nm)	Pore volume (cm^3/g)
NBT4900	132.9	5.434	0.1806
NBT4901	101.2	22.97	0.5815
NBT4902	158.8	4.626	0.1837
NBT4903	80.75	20.17	0.4072

the grain boundary contribution is dominated towards the total resistive response of the compositions, hence, the total conductivity is also found to increase with the increase in Mg^{2+}-content in Bi-deficit NBT. Due to this doping effect, more oxygen vacancies are generated. And, thus, a huge amount of oxygen vacancy concentration is accountable for the superior oxide-ion transport inside the grains. Mg^{2+}-substitution reduces the blocking of grain boundaries [29]. Nevertheless, on substitution with more than 2 mol% of Mg^{2+} in Bi-deficit NBT, the bulk conductivity was found to decrease probably due to the association of vacancy-defect pairs and lesser solubility limit of Mg^{2+}. The defect pair complexes $[(Mg''_{Ti} - V_O^{\cdot\cdot})^{\times}]$ formation decreases the concentration of free oxygen vacancies by acting as internal sink [24,61].

4. Conclusions

The present study reports the first time synthesis of Bi deficit Mg^{2+}-doped sodium bismuth titanate perovskite compositions $Na_{0.5}Bi_{0.49}Ti_{(1-x)}Mg_{(x)}O_{3-\delta}$ (x = 0.00, 0.01, 0.02, 0.03) via polyol mediated route. This route of preparation helps to produce fine particles, better surface area and good conductivity at relatively lower processing temperatures as compared to solid-state reaction route. The Mg^{2+} doping at Ti^{4+} site improved the sintering behavior and also augmented the grain size. The phase formation of the investigated compositions was verified by the X-ray Rietveld refinement techniques confirms the rhombohedral symmetries with *R3c* space group. Structure-property correlation is established to explain the conductivity behavior of Bi deficient Mg^{2+}-doped sodium bismuth titanate compositions. The oxide ion migration behavior and electron density distribution map were analyzed by using the Room Temperature X-ray Rietveld refined Crystallographic data. Raman analysis reveals that the conductivity and the octahedron distortion are proportional, and this structural anisotropy helps in the migration. The maximum conductivity was observed for NBT4902 composition over the entire temperature range. Though at higher doping of Mg^{2+} (x > 0.02) the conductivity was found to slightly decrease, this may be due to the solubility limit of Mg^{2+} and association of Mg^{2+} defect-vacancies pairs. The structural, thermal, micro-structural, textural and migration studies like RAMAN, FTIR, TGA, BET

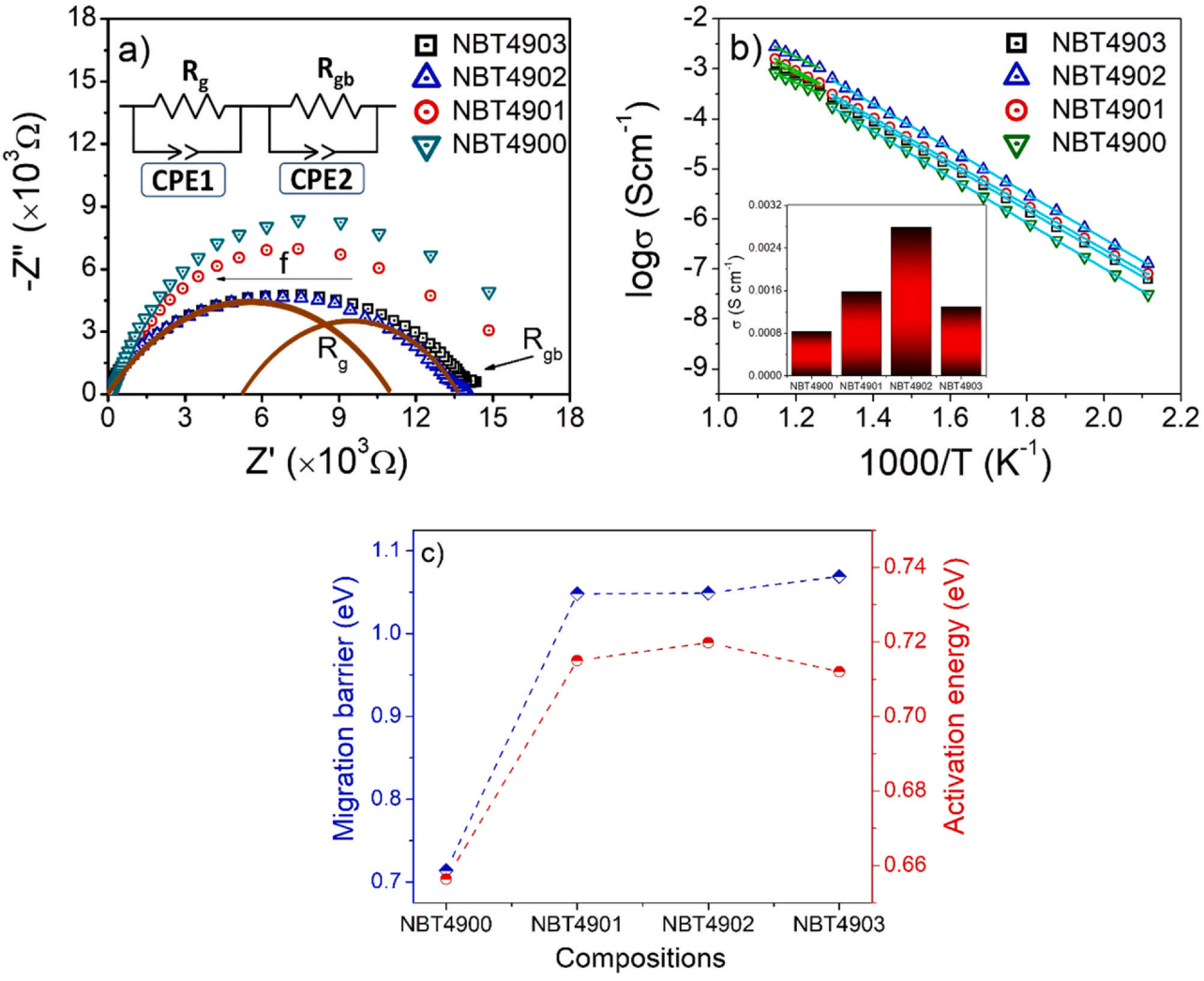

Fig. 12. (a) Representative AC impedance spectra at 500 °C. Inset in the figure shows corresponding equivalent circuit (b) Arrhenius plot for total conductivity. Inset shows the conductivity histogram at 600 °C (c) Variation of migration barrier and activation energy for $Na_{0.5}Bi_{0.49}Ti_{(1-x)}Mg_{(x)}O_{3-\delta}$ (x = 0.00, 0.01, 0.02, 0.03).

surface area, density and ion diffusion pathway analyses are also supported the conduction behavior of the investigated samples.

CRediT authorship contribution statement

Pragati Singh: Methodology; Investigation; Conceptualization; Formal analysis; Validation; Visualization; Software, Roles/Writing - original draft, Writing - review & editing. **Raghvendra Pandey:** Conceptualization; Data curation; Formal analysis; Roles/Writing - original draft; Software; Funding acquisition, Writing - review & editing. **Prabhakar Singh:** Writing - review & editing; Resources; Software; Supervision; Validation; Visualization; Funding acquisition; Project administration.

Declaration of competing interest

The authors declare that they have no known competing financial interests or personal relationships that could have appeared to influence the work reported in this paper.

Acknowledgements

The DST-FIST departmental funding partially supports this work through the project grant number (SR/FST/PSI-203/215(C)). One of the author's, R. Pandey, acknowledge the support of DST-SERB for the ECRA project (ECR/2016/001152).

Appendix A. Supporting information

Supplementary data associated with this article can be found in the online version at doi:10.1016/j.jallcom.2020.158492.

References

[1] T. Yang, J. Wang, Y. Chen, K. An, D. Ma, T. Vogt, K. Huang, A combined variable-temperature neutron diffraction and thermogravimetric analysis study on a promising oxygen electrode, SrCo0.9Nb0.1O3-δ, for reversible solid oxide fuel cells, ACS Appl. Mater. Interfaces 9 (2017) 34855–34864, https://doi.org/10.1021/acsami.7b08697

[2] Y. Lu, H. Zhao, K. Li, X. Du, Y. Ma, X. Chang, N. Chen, K. Zheng, K. Świerczek, Effective calcium doping at the B-site of BaFeO3-: δ perovskite: towards low-cost and high-performance oxygen permeation membranes, J. Mater. Chem. A 5 (2017) 7999–8009, https://doi.org/10.1039/c7ta00907k

[3] M.L. Tate, D.A. Blom, M. Avdeev, H.E.A. Brand, G.J. McIntyre, T. Vogt, I.R. Evans, New apatite-type oxide ion conductor, Bi2La8[(GeO4)6]O3: structure, properties, and direct imaging of low-level interstitial oxygen atoms using aberration-corrected scanning transmission electron microscopy, Adv. Funct. Mater. 27 (2017) 1605625, https://doi.org/10.1002/adfm.201605625

[4] S. Fop, E.J. Wildman, J.T.S. Irvine, P.A. Connor, J.M.S. Skakle, C. Ritter, A.C. McLaughlin, Investigation of the relationship between the structure and conductivity of the novel oxide ionic conductor Ba3MoNbO8.5, Chem. Mater. 29 (2017) 4146–4152, https://doi.org/10.1021/acs.chemmater.7b01298

[5] S.S. Pramana, T. Baikie, T. An, M.G. Tucker, J. Wu, M.K. Schreyer, F. Wei, R.D. Bayliss, C.L. Kloc, T.J. White, A.P. Horsfield, S.J. Skinner, Correlation of local structure and diffusion pathways in the modulated anisotropic oxide ion conductor CeNbO4.25, J. Am. Chem. Soc. 138 (2016) 1273–1279, https://doi.org/10.1021/jacs.5b11373

[6] X. Xu, W. Wang, W. Zhou, Z. Shao, Recent advances in novel nanostructuring methods of perovskite electrocatalysts for energy-related applications, Small Methods 2 (2018) 1800071, https://doi.org/10.1002/smtd.201800071

[7] S. Sanna, V. Esposito, J.W. Andreasen, J. Hjelm, W. Zhang, T. Kasama, S.B. Simonsen, M. Christensen, S. Linderoth, N. Pryds, Enhancement of the chemical stability in confined δ -Bi2O3, Nat. Mater. 14 (2015) 500–504, https://doi.org/10.1038/nmat4266

[8] R.J. Packer, S.J. Skinner, Remarkable oxide ion conductivity observed at low temperatures in a complex superstructured oxide, Adv. Mater. 22 (2010) 1613–1616, https://doi.org/10.1002/adma.200902692

[9] P.R. Slater, J.E.H. Sansom, J.R. Tolchard, Development of apatite-type oxide ion conductors, Chem. Rec. 4 (2004) 373–384, https://doi.org/10.1002/tcr.20028

[10] A.R. Genreith-Schriever, P. Hebbeker, J. Hinterberg, T. Zacherle, R.A. De Souza, Understanding oxygen-vacancy migration in the fluorite oxide CeO2: an ab initio study of impurity-anion migration, J. Phys. Chem. C 119 (2015) 28269–28275, https://doi.org/10.1021/acs.jpcc.5b07813

[11] T. Liu, X. Zhang, X. Wang, J. Yu, L. Li, A review of zirconia-based solid electrolytes, Ionics 22 (2016) 2249–2262, https://doi.org/10.1007/s11581-016-1880-1

[12] Y.J. Leng, S.H. Chan, S.P. Jiang, K.A. Khor, Low-temperature SOFC with thin film GDC electrolyte prepared in situ by solid-state reaction, Solid State Ion. 170 (2004) 9–15, https://doi.org/10.1016/j.ssi.2004.02.026

[13] M. Feng, J.B. Goodenough, K. Huang, C. Milliken, Fuel cells with doped lanthanum gallate electrolyte, J. Power Sources 63 (1996) 47–51, https://doi.org/10.1016/S0378-7753(96)02441-X

[14] A. Slodczyk, P. Colomban, S. Upasen, F. Grasset, G. André, Structural stability of anhydrous proton conducting SrZr0.9Er0.1O3-δ perovskite ceramic vs. protonation/deprotonation cycling: neutron diffraction and Raman studies, J. Phys. Chem. Solids 83 (2015) 85–95, https://doi.org/10.1016/j.jpcs.2015.03.025

[15] A. Smith, This is a Reproduction of a Library Book that was Digitized by Google as Part of an Ongoing Effort to Preserve the Information in Books and Make it Universally Accessible. https://books.google.com, Oxford Univ. XXX, 1986, 60. https://books.googleusercontent.com/books/content?req=AKW5QaeZb8cCzWl4I5L5LPrBClSJJgAXxJxciOIe9Nj7iGbkyHgkrSKm9_f_eQZBmoPJ-LQQeri7eZdQbiBrACMUvmaqh8k5jh-CyOT97vEdjCbC9lZkltWgy565ZnSag8m-cDJYlEGvgQupUrfpQ872PWSk2UuDKmw2c-wbLtqk2HWF2lP_ywlLi4L6KmLa7khGsKsla.

[16] K.S. McCombie, E.J. Wildman, S. Fop, R.I. Smith, J.M.S. Skakle, A.C. McLaughlin, The crystal structure and electrical properties of the oxide ion conductor Ba3WNbO8.5, J. Mater. Chem. A 6 (2018) 5290–5295, https://doi.org/10.1039/c7ta08989a

[17] K. Fujii, Y. Esaki, K. Omoto, M. Yashima, A. Hoshikawa, T. Ishigaki, J.R. Hester, New perovskite-related structure family of oxide-ion conducting materials NdBaInO4, Chem. Mater. 26 (2014) 2488–2491, https://doi.org/10.1021/cm500776x

[18] M. Li, M.J. Pietrowski, R.A. De Souza, H. Zhang, I.M. Reaney, S.N. Cook, J.A. Kilner, D.C. Sinclair, A family of oxide ion conductors based on the ferroelectric perovskite Na0.5Bi0.5TiO3, Nat. Mater. 13 (2013) 31–35, https://doi.org/10.1038/nmat3782

[19] M. Li, H. Zhang, S.N. Cook, L. Li, J.A. Kilner, I.M. Reaney, D.C. Sinclair, Dramatic influence of A-site nonstoichiometry on the electrical conductivity and conduction mechanisms in the perovskite oxide Na0.5Bi0.5TiO3, Chem. Mater. 27 (2015) 629–634, https://doi.org/10.1021/cm504475k

[20] K. Huang, M. Feng, J.B. Goodenough, Sol-gel synthesis of a new oxide-ion conductor Sr- and Mg-doped LaGaO3 perovskite, J. Am. Ceram. Soc. 79 (1996) 1100–1104, https://doi.org/10.1111/j.1151-2916.1996.tb08554.x

[21] R.K. Singh, P. Singh, Synthesis of La0.9Sr0.1Ga0.8Mg0.2O3−δ electrolyte via ethylene glycol route and its characterizations for IT-SOFC, Ceram. Int. 40 (2014) 7177–7184, https://doi.org/10.1016/j.ceramint.2013.12.056

[22] B.C.H. Steele, Appraisal of Ce1-yGdyO2-y/2 electrolytes for IT-SOFC operation at 500°C, Solid State Ion. 129 (2000) 95–110, https://doi.org/10.1016/S0167-2738(99)00319-7

[23] H. Zhang, A.H.H. Ramadan, R.A. De Souza, Atomistic simulations of ion migration in sodium bismuth titanate (NBT) materials: towards superior oxide-ion conductors, J. Mater. Chem. A 6 (2018) 9116–9123, https://doi.org/10.1039/c8ta02545b

[24] L. Koch, S. Steiner, K.C. Meyer, I.T. Seo, K. Albe, T. Frömling, Ionic conductivity of acceptor doped sodium bismuth titanate: influence of dopants, phase transitions and defect associates, J. Mater. Chem. C 5 (2017) 8958–8965, https://doi.org/10.1039/c7tc03031b

[25] X. He, Y. Mo, Accelerated materials design of Na0.5Bi0.5TiO3 oxygen ionic conductors based on first principles calculations, Phys. Chem. Chem. Phys. 17 (2015) 18035–18044, https://doi.org/10.1039/c5cp02181b

[26] J.A. Dawson, H. Chen, I. Tanaka, Crystal structure, defect chemistry and oxygen ion transport of the ferroelectric perovskite, Na0.5Bi0.5TiO3: insights from first-principles calculations, J. Mater. Chem. A 3 (2015) 16574–16582, https://doi.org/10.1039/c5ta03705k

[27] Y. Jung, S. Choi, S.L. Kang, Effect of oxygen partial pressure on grain boundary structure and grain growth behavior in BaTiO3, Acta Mater. 54 (2006) 2849–2855, https://doi.org/10.1016/j.actamat.2006.02.025

[28] F. Yang, H. Zhang, L. Li, I.M. Reaney, D.C. Sinclair, High ionic conductivity with low degradation in A-site strontium doped non-stoichiometric sodium bismuth titanate perovskite, Chem. Mater. 28 (15) (2016) 5269–5273, https://doi.org/10.1021/acs.chemmater.6b02555

[29] R. Bhattacharyya, S. Das, S. Omar, High ionic conductivity of Mg2+-doped non-stoichiometric sodium bismuth titanate, Acta Mater. 159 (2018) 8–15, https://doi.org/10.1016/j.actamat.2018.08.007

[30] M. Li, M.J. Pietrowski, R.A. De Souza, H. Zhang, I.M. Reaney, S.N. Cook, J.A. Kilner, D.C. Sinclair, A family of oxide ion conductors based on the ferroelectric perovskite Na0.5Bi0.5TiO3, Nat. Mater. 13 (2014) 31–35, https://doi.org/10.1038/nmat3782

[31] Y. Lu, C.A. López, J. Wang, J.A. Alonso, C. Sun, Insight into the structure and functional application of Mg-doped Na0.5Bi0.5TiO3 electrolyte for solid oxide fuel cells, J. Alloy. Compd. 752 (2018) 213–219, https://doi.org/10.1016/j.jallcom.2018.04.037

[32] E.A. Reshetnikova, I.V. Lisnevskaya, A.I. Terekhin, Hydrothermal synthesis of sodium bismuth titanate ferroelectrics, Inorg. Mater. 56 (2020) 83–90, https://doi.org/10.1134/S0020168520010136

[33] M.M. Lencka, M. Oledzka, R.E. Riman, Hydrothermal Synthesis of Sodium and Potassium Bismuth Titanates, 12, 2000, 1323–1330. https://doi.org/10.1021/cm9906654.

[34] C.Y. Kim, T. Sekino, K. Niihara, Synthesis of bismuth sodium titanate nanosized powders by solution/sol-gel process, J. Am. Ceram. Soc. 86 (2003) 1464–1467, https://doi.org/10.1111/j.1151-2916.2003.tb03497.x

[35] M.V. Ramana, S.R. Kiran, N. Ramamanohar Reddy, K.V. Siva Kumar, V.R.K. Murthy, B.S. Murty, Synthesis of lead free sodium bismuth titanate (Nbt) ceramic by conventional and microwave sintering methods, J. Adv. Dielectr. 01 (2011) 71–77, https://doi.org/10.1142/s2010135×11000094
[36] J. Hao, X. Wang, R. Chen, L. Li, Synthesis of (Bi0.5Na0.5)TiO3 nanocrystalline powders by stearic acid gel method, Mater. Chem. Phys. 90 (2005) 282–285, https://doi.org/10.1016/j.matchemphys.2004.05.019
[37] X. Zhou, C. Jiang, C. Chen, H. Luo, K. Zhou, D. Zhang, Morphology control and piezoelectric response of Na0.5Bi0.5TiO3 synthesized via a hydrothermal method, CrystEngComm 18 (2016) 1302–1310, https://doi.org/10.1039/c5ce02248g
[38] H. Zhang, S. Jiang, J. Xiao, K. Kajiyoshi, Low temperature preparation and electrical properties of sodium-potassium bismuth titanate lead-free piezoelectric thick films by screen printing, J. Eur. Ceram. Soc. 30 (2010) 3157–3165, https://doi.org/10.1016/j.jeurceramsoc.2010.07.012
[39] D. Zhou, H. Li, S. Gong, Y. Hu, K. Han, Sodium bismuth titanate-based lead-free piezoceramics prepared by aqueous gelcasting, J. Am. Ceram. Soc. 91 (2008) 2792–2796, https://doi.org/10.1111/j.1551-2916.2008.02511.x
[40] S. Swain, P. Kumar, D.K. Agrawal, Sonia, dielectric and ferroelectric study of KNN modified NBT ceramics synthesized by microwave processing technique, Ceram. Int. 39 (2013) 3205–3210, https://doi.org/10.1016/j.ceramint.2012.10.005
[41] E.A. Reshetnikova, I.V. Lisnevskaya, E.A. Zalyubovskaya, V.V. Butova, A.V. Soldatov, The effect of hydrothermal synthesis parameters on the formation of sodium bismuth titanate, Comments Inorg. Chem. 40 (2020) 314–326, https://doi.org/10.1080/02603594.2020.1813728
[42] G. Cilaveni, K.V. Ashok Kumar, S.S.K. Raavi, C. Subrahmanyam, S. Asthana, Control over relaxor, piezo-photocatalytic and energy storage properties in Na0.5Bi0.5TiO3 via processing methodologies, J. Alloy. Compd. 798 (2019) 540–552, https://doi.org/10.1016/j.jallcom.2019.05.235
[43] H. Chen, L.L. Wong, S. Adams, SoftBV – a software tool for screening the materials genome of inorganic fast ion conductors, Acta Crystallogr. Sect. B Struct. Sci. Cryst. Eng. Mater. 75 (2019) 18–33, https://doi.org/10.1107/S2052520618015718
[44] S. Adams, Modelling ion conduction pathways by bond valence pseudopotential maps, Solid State Ion. 136–137 (2000) 1351–1361, https://doi.org/10.1016/S0167-2738(00)00576-2
[45] K. Momma, F. Izumi, VESTA 3 for three-dimensional visualization of crystal, volumetric and morphology data, J. Appl. Crystallogr. 44 (2011) 1272–1276, https://doi.org/10.1107/S0021889811038970
[46] P. Singh, P.K. Jha, A.S.K. Sinha, P.A. Jha, P. Singh, Ion dynamics of non-stoichiometric Na0.5+xBi0.5-xTiO3-δ: a degradation study, Solid State Ion. 345 (2020) 115158, https://doi.org/10.1016/j.ssi.2019.115158
[47] D.K. Khatua, T. Mehrotra, A. Mishra, B. Majumdar, A. Senyshyn, R. Ranjan, Anomalous influence of grain size on the global structure, ferroelectric and piezoelectric response of Na0.5Bi0.5TiO3, Acta Mater. 134 (2017) 177–187, https://doi.org/10.1016/j.actamat.2017.05.068
[48] H. Mändar, J. Felsche, V. Mikli, T. Vajakas, AXES1.9: new tools for estimation of crystallite size and shape by Williamson-Hall analysis, J. Appl. Crystallogr. 32 (1999) 345–350, https://doi.org/10.1107/S0021889898011170
[49] S. Adams, From bond valence maps to energy landscapes for mobile ions in ion-conducting solids, Solid State Ion. 177 (2006) 1625–1630, https://doi.org/10.1016/j.ssi.2006.03.054
[50] E. Niwa, M. Yashima, Discovery of oxide-ion conductors with a new crystal structure, BaSc2- x AxSi3O10-x/2 (A = Mg, Ca) by screening Sc-containing oxides through the bond-valence method and experiments, ACS Appl. Energy Mater. 1 (2018) 4009–4015, https://doi.org/10.1021/acsaem.8b00701
[51] P. Singh, P.K. Jha, A.S.K. Sinha, P.A. Jha, P. Singh, Ion dynamics of non-stoichiometric Na0.5+xBi0.5-xTiO3-δ: a degradation study, Solid State Ion. 345 (2020) 115158, https://doi.org/10.1016/j.ssi.2019.115158
[52] M.K. Niranjan, T. Karthik, S. Asthana, J. Pan, U.V. Waghmare, Theoretical and experimental investigation of Raman modes, ferroelectric and dielectric properties of relaxor Na0.5Bi0.5TiO 3, J. Appl. Phys. 113 (2013) 0–7, https://doi.org/10.1063/1.4804940
[53] M.K. Niranjan, T. Karthik, S. Asthana, J. Pan, U.V. Waghmare, Theoretical and experimental investigation of Raman modes, ferroelectric and dielectric properties of relaxor Na0.5Bi0.5TiO 3, J. Appl. Phys. 113 (2013) 194106, https://doi.org/10.1063/1.4804940
[54] D.E. Jain Ruth, B. Sundarakannan, Structural and Raman spectroscopic studies of poled lead-free piezoelectric sodium bismuth titanate ceramics, Ceram. Int. 42 (2016) 4775–4778, https://doi.org/10.1016/j.ceramint.2015.11.162
[55] R. Selvamani, G. Singh, V. Sathe, V.S. Tiwari, P.K. Gupta, Dielectric, structural and Raman studies on (Na0.5Bi0.5TiO3)(1−x)(BiCrO3)x ceramic, J. Phys. Condens. Matter 23 (2011) 055901, https://doi.org/10.1088/0953-8984/23/5/055901
[56] K.S.W. Sing, D.H. Everett, R.A.W. Haul, L. Moscou, R.A. Pierotti, J. Rouquerol, T. Siemieniewska, Internationalunion of pure commission on colloid and surface chemistry including catalysisreporting physisorption data for gas/solid systems with special reference to the determination of surface area and porosity, Pure Appl. Chem. 57 (1985) 603–619.
[57] F. Yang, P. Wu, D.C. Sinclair, Enhanced bulk conductivity of A-site divalent acceptor-doped non-stoichiometric sodium bismuth titanate, Solid State Ion. 299 (2016) 38–45, https://doi.org/10.1016/j.ssi.2016.09.016
[58] P.A.R. West, Oxide Ion Conduction in A-site Bi-containing Perovskite-type Ceramics By, 2016.
[59] F. Yang, M. Li, Optimisation of oxide-ion conductivity in acceptor-doped Na0.5Bi0.5TiO3 perovskite: approaching the limit, J. Mater. Chem. A 5 (2017) 21658–21662, https://doi.org/10.1039/C7TA07667C
[60] M. Saiful Islam, Ionic transport in ABO3 perovskite oxides: a computer modelling tour, J. Mater. Chem. 10 (2000) 1027–1038, https://doi.org/10.1039/a908425h
[61] K.C. Meyer, K. Albe, Influence of phase transitions and defect associates on the oxygen migration in the ion conductor Na1/2Bi1/2TiO3, J. Mater. Chem. A 5 (2017) 4368–4375, https://doi.org/10.1039/c6ta10566a